



Evidence for Enhanced Eddy Mixing at Middepth in the Southern Ocean

K. SHAFER SMITH

Center for Atmosphere Ocean Science, Courant Institute of Mathematical Sciences, New York University, New York, New York

JOHN MARSHALL

Department of Earth, Atmospheric and Planetary Sciences, Massachusetts Institute of Technology, Cambridge, Massachusetts

(Manuscript received 16 July 2007, in final form 12 June 2008)

ABSTRACT

Satellite altimetric observations of the ocean reveal surface pressure patterns in the core of the Antarctic Circumpolar Current (ACC) that propagate downstream (eastward) but slower than the mean surface current by about 25%. The authors argue that these observations are suggestive of baroclinically unstable waves that have a steering level at a depth of about 1 km. Detailed linear stability calculations using a hydrographic atlas indeed reveal a steering level in the ACC near the depth implied by the altimetric observations. Calculations using a nonlinear model forced by the mean shear and stratification observed close to the core of the ACC, coinciding with a position where mooring data and direct eddy flux measurements are available, reveal a similar picture, albeit with added details. When eddy fluxes are allowed to adjust the mean state, computed eddy kinetic energy and eddy stress are close to observed magnitudes with steering levels between 1 and 1.5 km, broadly consistent with observations.

An important result of this study is that the vertical structure of the potential vorticity (PV) eddy diffusivity is strongly depth dependent, implying that the diffusivity for PV and buoyancy are very different from one another. It is shown that the flow can simultaneously support a PV diffusivity peaking at $5000 \text{ m}^2 \text{ s}^{-1}$ or so near the middepth steering level and a buoyancy diffusivity that is much smaller, of order $1000 \text{ m}^2 \text{ s}^{-1}$, exhibiting less vertical structure. An effective diffusivity calculation, using an advected and diffused tracer transformed into area coordinates, confirms that the PV diffusivity more closely reflects the mixing properties of the flow than does the buoyancy diffusivity, and points explicitly to the need for separating tracer and buoyancy flux parameterizations in coarse-resolution general circulation models. Finally, implications for the eddy-driven circulation of the ACC are discussed.

1. Introduction

Mixing and stirring due to mesoscale eddies in the ocean exhibit considerable variability in space and time. For example, studies by Holloway (1986), Stammer (1998), Bauer et al. (2002), and Marshall et al. (2006) using surface altimetry suggest significant horizontal spatial variation in eddy diffusivity at the ocean's surface. Studies of the vertical structure of mixing and stirring, however, are more sparse and challenging. The studies of Phillips and Rintoul (2000) and Gille (2003) find depth dependence in the eddy statistics, but such estimates are based on isolated moorings and sparsely distributed subsurface floats.

There is no feasible way at present to attain sufficiently resolved direct observations of eddy diffusivity and mixing rates at depth over significant regions of the ocean, so one must use indirect methods and models. Ferreira et al. (2005), for example, use inverse methods to back out eddy diffusivities from a data assimilation model. The inferred eddy stress is computed as the residual necessary to minimize the difference between the observed global temperature–salinity distribution of the ocean and the model. The magnitudes of mixing rates found in that study are consistent with other studies (e.g., Marshall et al. 2006) and are strongly depth dependent. Here we draw on additional evidence that is strongly suggestive of depth-dependent mixing.

Mesoscale eddies are widely believed to be generated by baroclinic instability of the mean flow (Gill et al. 1974; Robinson and McWilliams 1974; Stammer 1997; Smith 2007), extracting their energy from the stores of

Corresponding author address: K. Shafer Smith, Center for Atmosphere Ocean Science, New York University, 251 Mercer Street, New York, NY 10012.
E-mail: shafer@cims.nyu.edu

Deep eddy mixing in the Southern Ocean

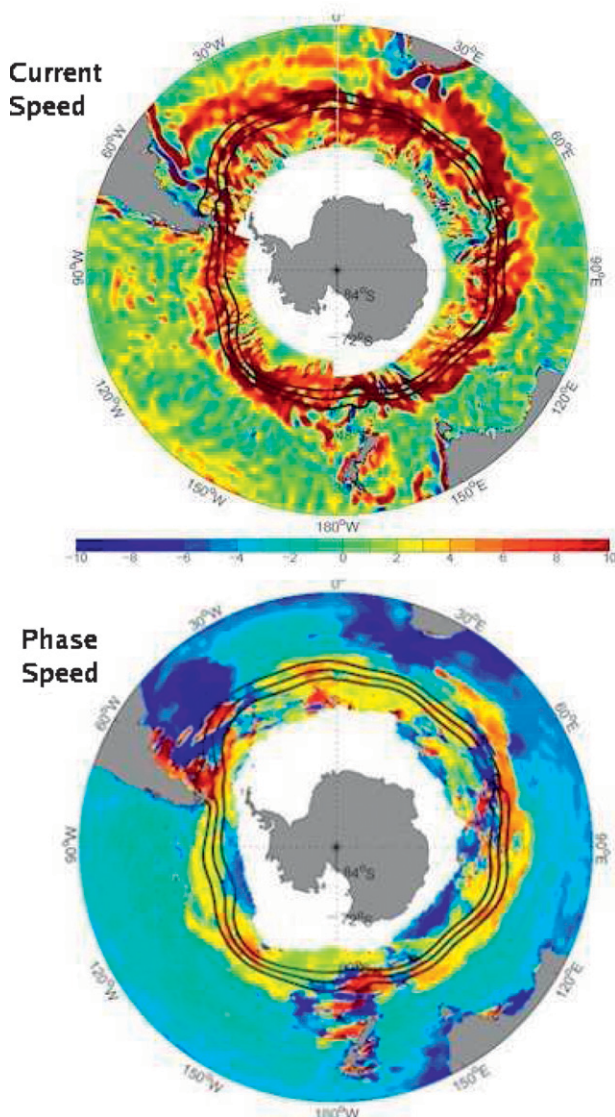


FIG. 1. (a) Climatological zonal current speed in cm s^{-1} at the surface as measured by surface drifters (courtesy of N. Maximenko). Positive is eastward, and the thick black lines are isopleths of a climatological surface geostrophic streamfunction inferred from altimetry, chosen to delineate that part of the flow that in a mean sense is circumpolar. (b) Zonal phase speed of surface pressure signals computed from altimetric observations (courtesy of C. Hughes).

available potential energy in the mean oceanic density structure. Rossby waves, owing their existence to mean potential vorticity (PV) gradients, mutually interact with one another and, in strongly unstable flows, grow to finite amplitude, exciting turbulent cascades. Even weakly unstable flows can lead to turbulence and the production of coherent vortices. In either case the process starts with the linear growth of a few waves. For

unstable zonal flows, the real part of the Doppler-shifted phase speed $c_r - U(z)$ will vanish somewhere in the flow. If the instability is weak ($c_i \ll c_r$), the disturbance will be localized around the level at which $c_r - U(z)$ vanishes—the steering level or critical layer. At this depth, the growing wave can efficiently displace fluid parcels large meridional distances, resulting in enhanced mixing of fluid parcels and their conserved properties (such as conservative tracers and PV)—see, for example, Green (1970). In more strongly unstable flow, characterized by an energy cascade and a spectrum of continuously excited waves, the exact theoretical importance of the steering level of the linearly most unstable mode is less clear. Nevertheless, its depth is likely a place of active eddy stirring and mixing. For example, Lozier and Bercovici (1992) present evidence, from both linear and nonlinear analysis, for enhanced particle exchange at the steering level.

Satellite altimetric observations of the Southern Ocean do suggest the presence of large-scale waves that propagate downstream in the Antarctic Circumpolar Current (ACC) at a rate significantly slower (25%) than that of surface currents. This was anticipated by Hughes (1996) in studies of an eddy-resolving model of the Southern Ocean where it was argued that the eastward flow of the ACC turned it into a Rossby waveguide. The top panel of Fig. 1 shows observations of surface geostrophic flow from surface drifter observations (N. Maximenko 2007, personal communication). We see that the surface flow associated with the ACC is directed eastward, peaking at a speed of about 8 cm s^{-1} . This is consistent with the analysis by Karsten and Marshall (2002) of streamwise-average buoyancy and geostrophic flow (shown in Fig. 3) obtained by vertical integration of the thermal wind equation, assuming a level of no motion at the bottom of the ocean (note that ACC transport is sensitive to the assumption of a level of no motion, but near-surface currents are much less so).

The bottom panel of Fig. 1 shows an estimate of “wave speed” c_r (C. Hughes 2007, personal communication).¹ The apparent phase speed is $c_r \sim 2 \text{ cm s}^{-1}$ over the latitudinal range of the ACC (roughly 50° –

¹ The wave speed is calculated as follows: The altimetric time series is filtered at each point, passing periods between 7 and 57 weeks. A running mean over 10° of longitude is subtracted to ensure that only wavelengths shorter than about 10° are measured. Each time series is divided by its standard deviation and a Radon transform is performed on the 5° (longitude) patch centered on each grid point to calculate speed for that grid point—the chosen speed is that giving the maximum Radon transform. Each latitude is treated independently. A 540-week time series is used.

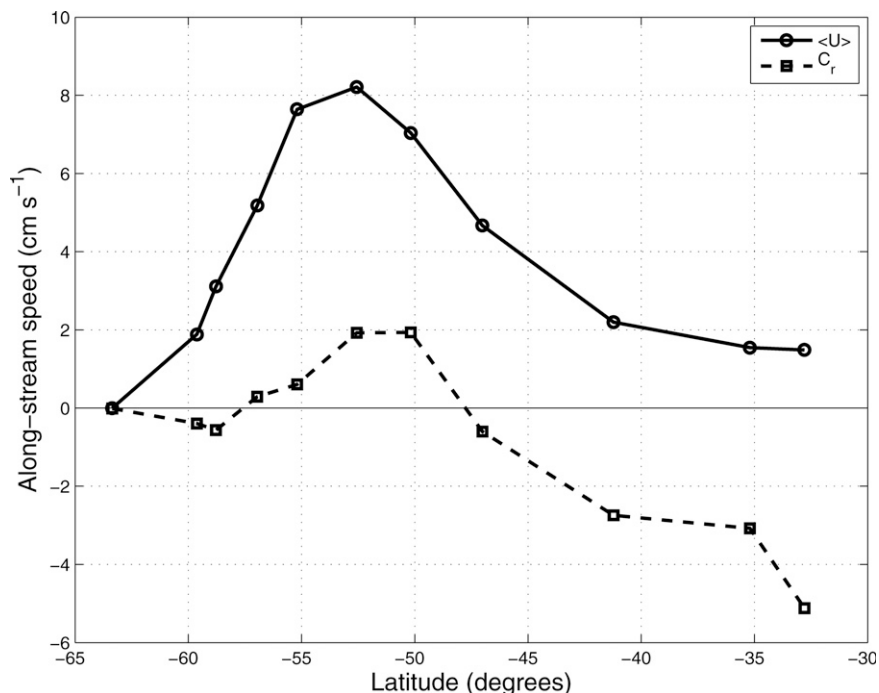


FIG. 2. Streamwise average of along-stream current, U_{surface} , and altimetric wave speed, c_r (positive is eastward), in cm s^{-1} .

55°S); it is directed downstream but at a speed much less than the surface current. The wavelengths are of order 100–300 km, consistent with baroclinic planetary waves being advected eastward by the mean current.² Equatorward of the ACC the waves travel from east to west, as is found in the rest of the oceanic basins (Chelton and Schlax 1996). Both the alongstream average current and the wave speeds are plotted in Fig. 2 to summarize the observations. The vertical structure of the mean current, shown in Fig. 3, along with the wave speed observations in Fig. 2 suggest that the steering level is at a depth of about 1 km.

An analysis of the stability properties of the global hydrography by Smith (2007) also reveals indirect evidence of deep eddy mixing in the ACC. In that paper, it is shown that mean PV gradients exhibit multiple zero crossings in the vertical. There are both vigorous, near-surface instabilities and slower, thermocline-level baroclinic instabilities associated with interior PV gradients. The steering level of these latter modes is

² Chelton et al. (2007) and collaborators have recent evidence that what appear to be waves may actually be coherent vortices being advected by the mean flow. In either case, the difference in speed between the wave, or eddy motion, and the mean flow lead us to consider what happens at depths where these speeds are equal.

found to lie at a level where PV gradients change sign. In the ACC this occurs at a depth of a kilometer or so, and is consistent with phase speeds observed from altimetry. Moreover, the linear stability analysis shows that baroclinic growth in the ACC is dominated by waves with peak energy conversion at about 1-km depth (see Fig. 4).

Our goals here are to (i) understand why the steering level is at a depth of about 1 km and (ii) study the implications of this deep steering level for eddy-driven processes in the ACC. We address these goals with the aid of a local process model that we use to “measure” eddy fluxes. The model is quasigeostrophic (QG) and horizontally periodic, but uses the mean hydrography (shear and stratification) of a location that is coincident with the field study of Phillips and Rintoul (2000, hereafter PR00). PR00 compute eddy stress, energy, and flux, using an array of direct current measurements in a location just south of Tasmania, in the core of the ACC. We use their measured estimates as a benchmark against which to compare our modeled eddy statistics.

A crucial result of our study is that mesoscale eddy mixing is, indeed, peaked at a depth of about 1 km in the core of the ACC. Moreover, mixing is found to be strongly depth dependent, and the diffusivities for buoyancy and potential vorticity are found to be quite

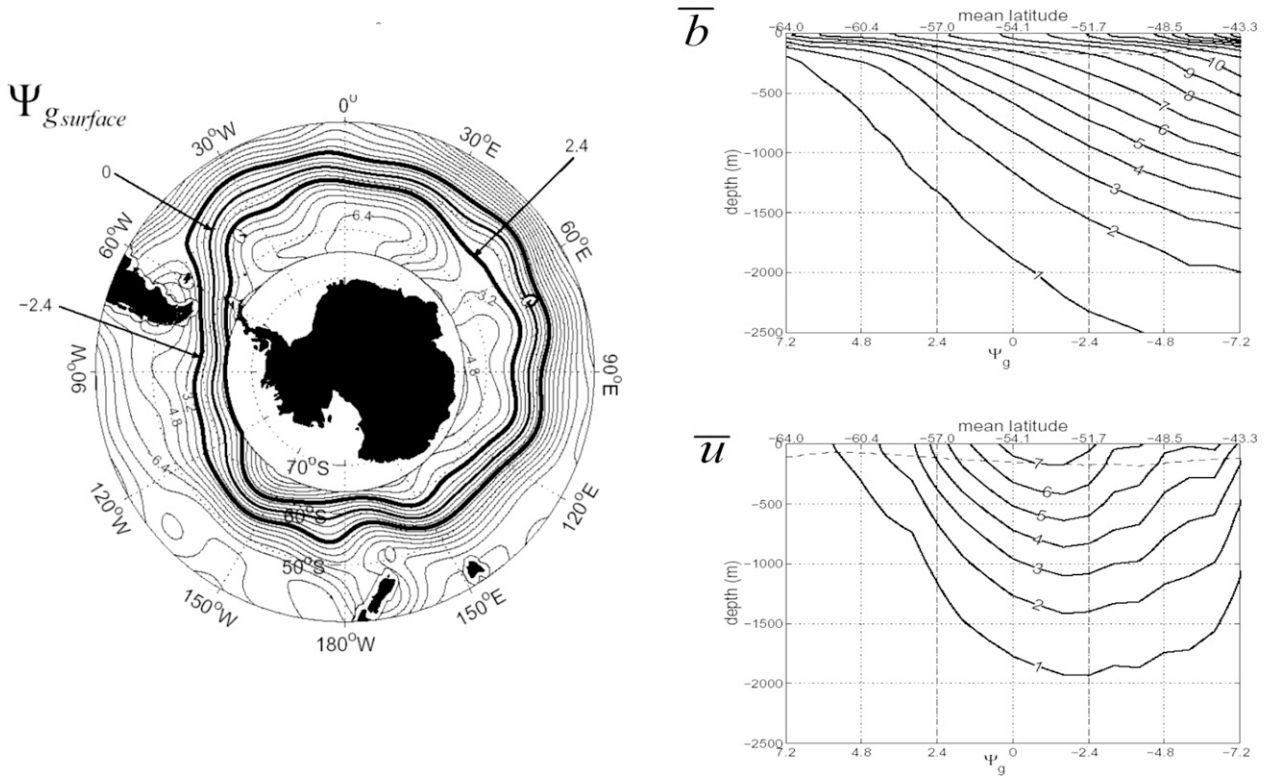


FIG. 3. (left) Time-mean geostrophic streamfunction measured from altimetry; (top right) mean streamwise-average buoyancy with contour interval 10^{-3} m s^{-2} ; (bottom right) mean streamwise-average thermal wind velocity with contour interval 1 cm s^{-1} obtained by assuming that the zonal flow at the bottom is zero and integrating up using thermal wind. The vertical dashed lines mark the boundaries of the ACC; the horizontal dashed line marks the annual mean mixed layer depth. Modified from Karsten and Marshall (2002).

different, both in magnitude and structure (basic kinematics show that, when mixing is not constant in the vertical, diffusivities of buoyancy and PV cannot be the same). An effective diffusivity calculation (Nakamura 1996) additionally suggests that tracers are mixed more like PV than like buoyancy, though differences are present. This has obvious implications for numerical models that must parameterize the transfer and mixing of properties by mesoscale eddies.

The paper is organized as follows: In section 2, we connect the surface observations to a linear baroclinic instability analysis using the hydrography of the Southern Ocean and review connections to eddy transfer. In section 3, we focus on the target region of the observational analysis of PR00. Here we compute both detailed linear and nonlinear solutions and calibrate our results to the measurements of PR00. The model eddy stresses and diffusivities are analyzed in section 4 and are shown to be consistent with observations of eddy stress and diffusivity. In section 5, we summarize and discuss the implications of our study for eddy parameterization in coarse-resolution general circulation models and for the dynamics of the ACC.

2. Interpretation in terms of linear baroclinic instability theory

Recently linear baroclinic instability theory has been systematically applied to the hydrographic structure of the ocean to map stability properties of the flow (see Killworth and Blundell 2007; Smith 2007). Here we specialize key results of the latter paper to the Southern Ocean and discuss their implications for the observations presented in section 1. The details of the stability problem are discussed in Smith (2007), but we briefly review key elements of the method below.

Neutral density $\bar{\rho}$ (Jackett and McDougall 1997) is computed from the Gouretski and Koltermann (2004, hereafter GK04) hydrographic climatology, and the thermal wind velocity is then computed at each horizontal position from density gradients via

$$f \frac{\partial \mathbf{U}}{\partial z} = \mathbf{z} \times \nabla B, \quad (2.1)$$

where $\mathbf{U} = (U, V)$ are the horizontal components of the mean geostrophic flow, f is the Coriolis parameter, and $B = -g\bar{\rho}/\rho_0$ is the mean (neutral) buoyancy. The mean

Deep eddy mixing in the Southern Ocean
Critical Layer Depth (m)

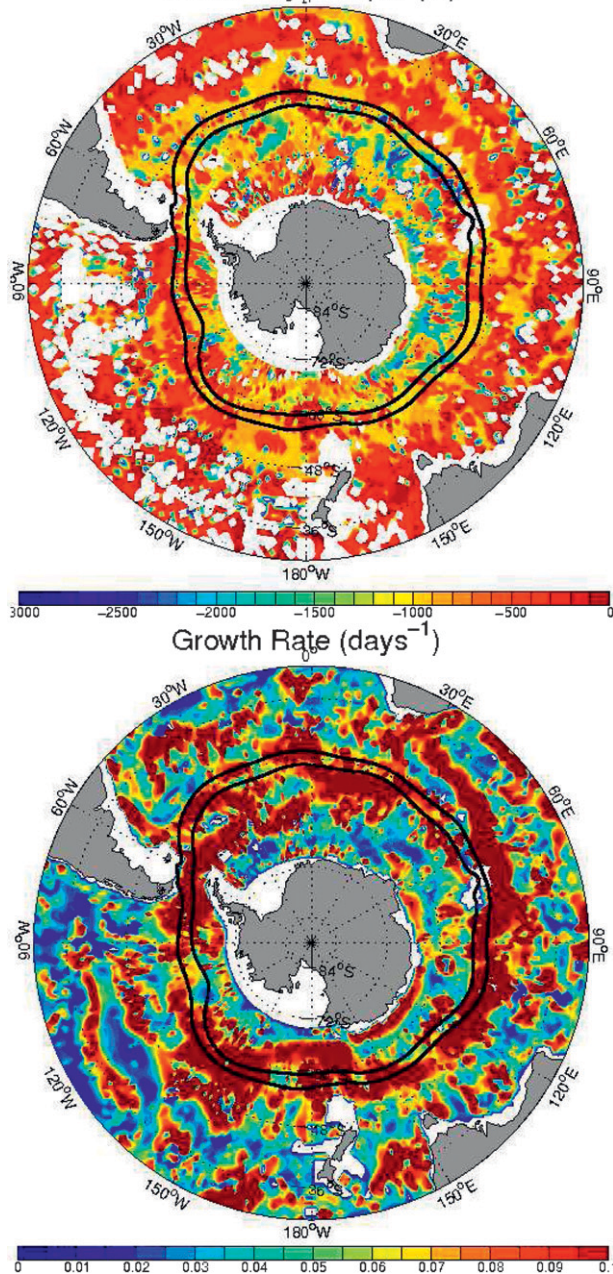


FIG. 4. (a) Critical layer depth (m) corresponding to the fastest-growing, baroclinically unstable mode, filtered by the requirement that the energy transfer of the mode be at least $5 \times 10^{-4} \text{ W m}^{-2}$ (the white areas indicate regions that do not satisfy this criterion); (b) growth rate for same calculation (days^{-1}). The thick black lines delineate the core of the ACC.

velocity and stratification are taken to be horizontally local and slowly varying in the sense of Pedlosky (1984); hence each horizontal location only depends on z . Consistent with the assumption of a slowly varying

background state that is locally horizontally homogeneous, the domain is taken to be horizontally periodic. This implies the neglect of mean relative vorticity, which is well justified by the smallness of horizontal gradients of the geostrophic velocities computed from hydrography (see also Smith, 2007).

A local linear stability calculation is performed at each horizontal location. Substitution of a plane wave solution of the form $\psi' = \text{Re}\{\tilde{\psi}(z) \exp[i(kx + ly - \omega t)]\}$, where $\tilde{\psi}$ is the complex amplitude, into the QG equations gives

$$(\mathbf{K} \cdot \mathbf{U} - \omega)(\Gamma - |\mathbf{K}|^2)\tilde{\psi} = -\Pi\tilde{\psi}, \quad -H < z < 0, \quad (2.2a)$$

$$\begin{aligned} (\mathbf{K} \cdot \mathbf{U} - \omega)\tilde{\psi}_z &= \left(\mathbf{K} \cdot \frac{d\mathbf{U}}{dz} - \frac{N^2}{f} \mathbf{z} \times \nabla h_B \right) \tilde{\psi}, \\ z &= -H, 0, \end{aligned} \quad (2.2b)$$

where $\Gamma = \partial/\partial_z(f^2/N^2)\partial/\partial_z$ (an operator), $\mathbf{K} = (k, l)$ is the horizontal wavenumber, h_b is the bottom topography and $\Pi = \hat{\mathbf{z}} \cdot (\mathbf{K} \times \nabla Q)$.³ The horizontal quasigeostrophic potential vorticity (QGPV) gradient is given by

$$\nabla Q = \beta \mathbf{y} - f \frac{\partial \mathbf{S}}{\partial z}, \quad (2.3)$$

where β is the planetary vorticity gradient and $\mathbf{S} = -\nabla B/B_z$ is the slope of buoyancy surfaces. The linear eigenvalue problem (2.2) is solved on a grid of horizontal wavenumbers ranging in modulus from 1/10 to 100 times the local first deformation wavenumber. From the solution, the modes with imaginary phase speeds are filtered to require an energetic conversion rate that is of the same order as the winds. In particular, the amplitude of each raw unstable mode is dimensionalized with an eddy velocity of 0.1 m s^{-1} , the corresponding rate at which mean available potential energy is transferred to eddy kinetic energy via each mode is computed, and only those modes with conversion exceeding 0.5 mW m^{-2} (typical wind input is about 1 mW m^{-2}) are considered (see Smith 2007, and references therein, for more detail). This has the effect of removing very small scale surface layer modes that, while potentially important in mixed layer dynamics, have little energetic influence on the large-scale mean state.

a. Critical layers and growth rates from linear theory

If the observed undulations at the surface of the ACC are the expression of baroclinic waves with a criti-

³ Note that we use \mathbf{K} (and K) for horizontal wavenumber, not to be confused with diffusivity, denoted by κ .

cal level in the interior, then by the Miles–Howard theorem (Howard 1961), these waves are unstable. By considering the real parts of the phase speeds that correspond to the fastest-growing modes of energetic significance, we can compute the normal-mode critical-level directly. Specifically, the depth z_c of the critical layer will be such that

$$c_r - \mathbf{U}(z_c) \cdot \frac{\mathbf{K}_{\max}}{|\mathbf{K}_{\max}|} = 0,$$

where $\mathbf{K}_{\max} = (k_{\max}, l_{\max})$ is the local wavenumber of fastest growth. This form takes into account that the local mean flow is, in general, nonzonal, so the direction of fastest growth may have $l_{\max} \neq 0$.

Figure 4 shows the growth rate and steering level of the fastest-growing mode obtained by carrying out the stability analysis described above. The steering level of the fastest-growing mode, shown in Fig. 4a, is at a depth $O(1 \text{ km})$, consistent with the observations of U and c_r reviewed in the introduction. On the equatorial flank of the ACC, where the phase speed is directed westward, the steering level shallows.

The growth rate (Fig. 4b) shows the axis of the ACC to be a region of vigorous instability, where in some locations growth rates reach $(2 \text{ days})^{-1}$. The scales of the fastest-growing mode are $O(10 \text{ km})$ (figure not shown here), much smaller than the scale of the most energetic eddies in the ACC (Stammer 1997; Chelton et al. 2007). This is discussed at length in Smith (2007), where it is argued that the observed scale is likely the result of an inverse cascade, consistent with Scott and Wang (2005). Nonlinear simulations presented later support this conclusion.

b. PV flux and eddy diffusivity in linear theory

Green (1970) proposed a theory for PV fluxes in horizontally homogeneous, baroclinically unstable flow based on the fastest-growing linear normal mode. This idea was further developed in a two-layer context by Marshall (1981) and as a full eddy parameterization scheme by Killworth (1997). The linear theory will not be formally correct in highly unstable flows and fully developed geostrophic turbulence, but it does provide a form to which one can compare measured and simulated fluxes. We briefly review this theory here. Using the linearly most unstable normal mode solutions from (2.2), one has

$$\overline{\mathbf{u}'q'} = \frac{1}{2} \text{Re}\{\tilde{\mathbf{u}}\tilde{q}^*\} = \mathbf{z} \times \mathbf{K} \frac{\omega_i}{2} \left| \frac{\tilde{\psi}}{\mathbf{K} \cdot \mathbf{U} - \omega} \right|^2 \Pi,$$

where the asterisk superscript denotes a complex conjugate, $\tilde{\mathbf{u}} = i\mathbf{z} \times \mathbf{K}\tilde{\psi}$, $\tilde{q} = (\Gamma - |\mathbf{K}|^2)\tilde{\psi}$, $\omega_i = \text{Im}\{\omega\}$, and

Π is defined below (2.2). Parseval's theorem is used in the first equality and (2.2a) is used in the second. This form is equivalent to Killworth's Eq. (30). In the case of a mean velocity that does not turn with depth and with $\beta \ll |f\partial_z(B_y/B_z)|$ (thus contributing negligibly to the mean PV gradient), ∇Q points perpendicular to mean streamlines at every depth (both of these assumptions are justified in the ACC). Projecting the PV flux onto the cross-stream direction (denoted by the unit vector \mathbf{n}), and assuming $\mathbf{K}_{\max} \perp \nabla Q$ (so that \mathbf{K}_{\max} is in the direction of streamlines, denoted by the unit vector \mathbf{s}) results in a simplification of the linear approximation of the PV flux; namely,

$$\mathbf{n} \cdot \overline{\mathbf{u}'q'} = -\kappa_{q,\text{lin}} \mathbf{n} \cdot \nabla Q, \quad \text{where} \quad \kappa_{q,\text{lin}} = \frac{\omega_i}{2} \left| \frac{\tilde{\psi}}{\mathbf{s} \cdot \mathbf{U} - c} \right|^2, \quad (2.4)$$

equivalent to downgradient diffusion with diffusivity $\kappa_{q,\text{lin}}$. This is equivalent to Green's Eq. (15). In the above expression it is to be understood that $\omega_i = \max(\omega_i)$ and c is the corresponding complex phase speed for this mode, with wavenumber \mathbf{K}_{\max} . At the critical level z_c , the denominator of the diffusivity expression takes on a minimum; hence, the diffusivity $\kappa_{q,\text{lin}}$ has a maximum. Linear theory and physical reasoning, therefore, lead one to expect a peak in mixing at the critical level, as originally discussed by Green (1970). We now investigate how well these ideas apply to measurements and a process model study at a particular location in the Southern Ocean.

3. Detailed analysis at a field observation site in the ACC

The observational analysis of eddy statistics by PR00 provides us with an opportunity to make a more detailed comparison between observations and theory. Here we use the hydrography at the location of the PR00 analysis to compute both the linear stability characteristics of the region as well as the eddy fluxes in the nonlinearly equilibrated state that results from active baroclinic instability.

a. Local linear calculation

The linear stability computation discussed now is similar to that carried out for the same region in Smith (2007) (and for which the general method was reviewed in section 2), albeit here we first average profiles of mean velocity and mean density over a $5^\circ \times 5^\circ$ horizontal region centered about 51°S , 141°E . We project the results onto along-stream and across-stream coordinates—the

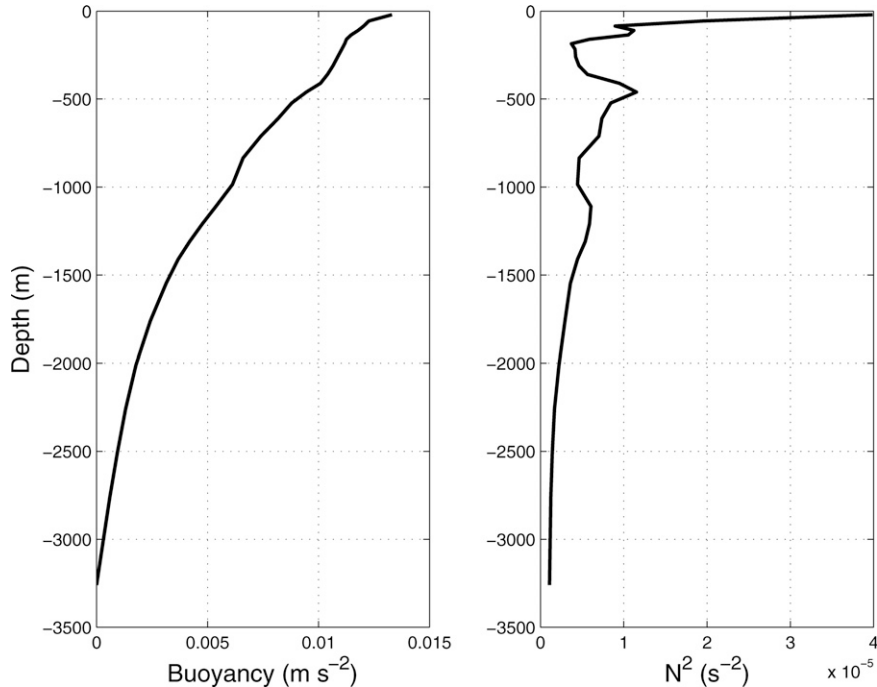


FIG. 5. (a) Neutral buoyancy $B = -(g/\rho_0)\bar{\rho}$ (m s^{-2}) and (b) neutral stratification $\partial B/\partial z = N^2$ (s^{-2}) at 51°S , 141°E .

local flow at this location is roughly east-southeast at the surface, and the velocity does not turn with depth, so the mean velocity can be represented with a single profile. There are 29 usable depth levels in the atlas after averaging and removing regions of vanishing static stability. The mean PV gradient at the bottom level includes the averaged topographic slope, computed from the Smith and Sandwell (1997) dataset.

Figure 5 shows the mean buoyancy (B) and stratification ($\partial B/\partial z = N^2$) profiles from the neutral density field $\bar{\rho}$, and the thin lines in Fig. 6 show the along-stream velocity $\mathbf{s} \cdot \mathbf{U}$ (where \mathbf{s} is the unit vector directed along streamlines) and across-stream QGPV gradient $\mathbf{n} \cdot \nabla Q$ (the thick lines are discussed in the next section). The mean velocity is computed from the GK04 dataset, using a finite difference approximation of the thermal wind balance (2.1), averaged over the 5° region of the target area. As is generically found at locations in the ACC, the mean across-stream QGPV gradient, computed from hydrography, is a complicated function of depth, with roughly five sign changes, and a magnitude of order 10–100 β (e.g., Marshall et al. 1993). It should be noted that (i) salinity measurements in the Southern Ocean are relatively sparse, so the neutral density field constructed from the GK04 dataset may be less accurate here than in other regions (S. Gille 2007, personal communication); (ii) relatively small changes

in the mean hydrography (particularly horizontal gradients, for which no optimization is performed in the construction of hydrographic datasets) lead to large changes in the mean QGPV gradient (which involves two vertical derivatives, and so brings out small-scale features); (iii) sharp reversals in the QGPV gradient lead to large levels of eddy energy production; and (iv) the use of shear coordinates by PR00 may introduce additional inaccuracies (Meinen and Luther 2003). We address these issues in the next section.

The growth rate as a function of along-stream wavenumber (nondimensionalized by the local first deformation wavenumber) that results from the full baroclinic stability calculation at this location is shown in Fig. 7. Three instability peaks are prominent, and the inset figures show the squared amplitudes $|\tilde{\eta}|^2$ corresponding to each of these: (i) the first (lowest wavenumber) peak occurs at a horizontal scale slightly larger than the first deformation scale of about 19 km and corresponds to a vertical structure that reflects a somewhat surface-intensified, top-to-bottom mode; (ii) the second peak, occurring at horizontal scales of about 5 km ($\sim R_d/4$), has a vertical structure focused in a sharp peak at about a depth of 1 km; (iii) the third peak, occurring at a horizontal scale of about 1 km, is trapped near the surface and associated with sharp gradients near the surface (note the change in ordinate in the

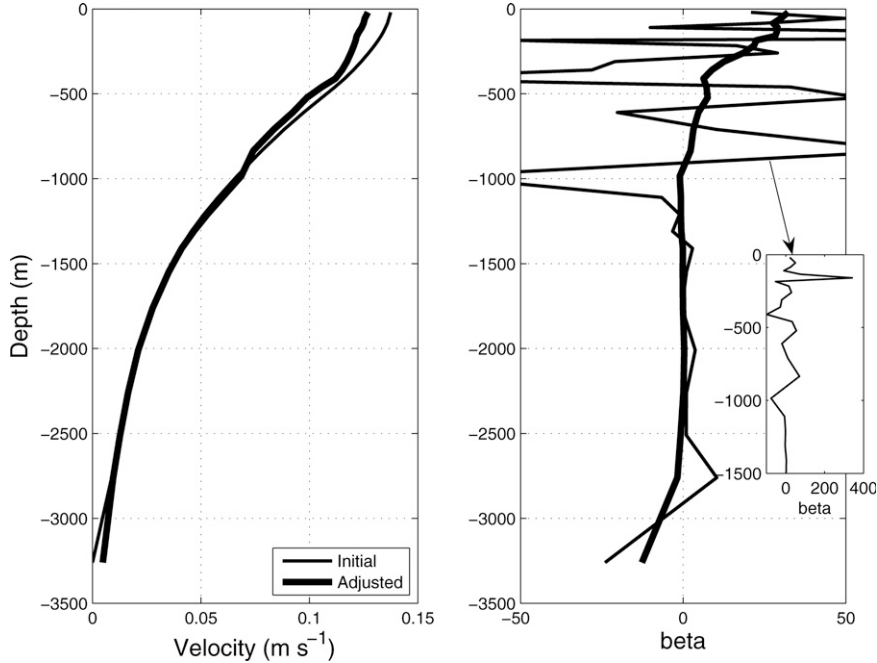


FIG. 6. (a) Streamwise velocity $\mathbf{U} \cdot \mathbf{s}$ (m s^{-1}) and (b) cross-stream QGPV gradient $\nabla Q \cdot \mathbf{n}$ (in units of $\beta = 1.45 \times 10^{-11} \text{ m}^{-1} \text{ s}^{-1}$ at 51°S , 141°E). The thin lines are the profiles computed directly from the thermal wind assuming a level of no motion at the bottom, and the thick lines are the steady-state profiles that evolve after adjustment by eddy fluxes via Eq. (3.1) in the nonlinear model. The inset plot in (b) is the hydrographic mean QGPV gradient for the upper 1500 m, shown over its full range of values.

inset plot). Note that the latter two instabilities have vertical structures concentrated right at the levels of reduced stratification, $\partial B/\partial z$, apparent in Fig. 5. The effects of these instabilities in generating steady-state eddy fluxes will now be addressed.

b. Nonlinear model

We now describe the results of a series of simulations with a nonlinear, doubly periodic spectral quasigeostrophic model. The model is used to simulate the fully developed turbulent state that results from the baroclinic instability of the same 29-level mean state for which the linear instabilities were computed in the previous section (the 29 depths available at the PR00 location from the GK04 dataset). The numerical model is the same as that used in Smith and Vallis (2002), albeit enabled to run in parallel on a distributed memory cluster, and with a few additions to the physics, described below. The scale of the model domain (largest resolved wavelength) is 1000 km, which allows sufficient room to equilibrate a field of eddies with length scales near those observed (80–120 km). The effective horizontal resolution is 256^2 , implying a smallest resolved wavelength of 3.9 km, or smallest resolved inverse wavenumber (radius) of less than 1 km. Dissipation of enstrophy

is accomplished with a highly scale selective exponential cutoff filter (Smith et al. 2002), so wavenumbers down to $k_{\text{cut}} = (2 \text{ km})^{-1}$ are modeled with no loss to the filter. Dissipation of energy occurs through a quadratic bottom drag (Grianiik et al. 2004; Arbic and Scott 2008), using $C_d = 10^{-3}$ and a bottom boundary layer depth of 10 m. Bottom relief for the target region is included from the Smith and Sandwell (1997) dataset by including its contribution to the bottom-level PV at each time step. The topographic section is made periodic by symmetrizing in both directions (the field is flipped in x , concatenated, and then the same is done in y). The mean slope of the topography in the target region is small (i.e., topographic β is less than the Coriolis gradient, which itself is already small compared to shear in the mean PV gradient), so the main influence of the topography is through its roughness, which is known to reduce the eddy energy somewhat (Treguier and Hua 1988).

The mean stratification and mean velocity profiles used in the model are the same as those used in the linear stability calculation of the previous subsection. Consistent with quasigeostrophic scaling, the buoyancy frequency is constant in time and horizontal space over the model domain. In a quasigeostrophic channel

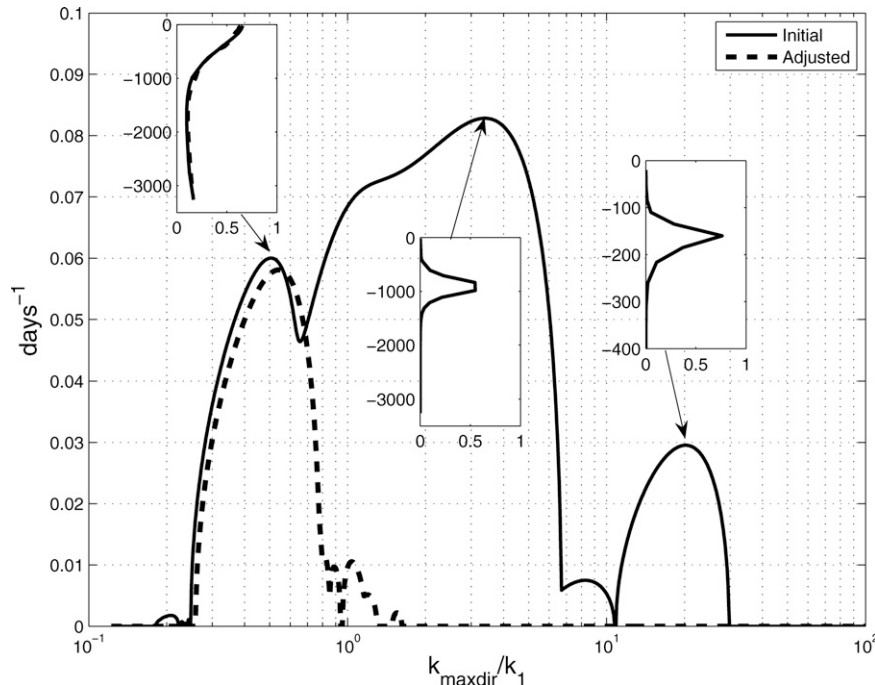


FIG. 7. Growth rate (days^{-1}) as a function of along-stream wavenumber (normalized by the first deformation wavenumber $K_d = 5.25 \times 10^{-5} \text{ m}^{-1}$, corresponding to a deformation radius of $R_d = 19 \text{ km}$) for the hydrographic mean state at 51°S , 141°E (solid line) and for the steady-state mean after adjustment by eddy fluxes (dashed line). The inset plots show the squared amplitude $|\psi|^2(z)$ for the three prominent peaks of the instability curve for the hydrographic mean state (the first inset also shows the squared amplitude for the peak instability of the adjusted mean state).

model, the zonal-mean velocity varies in time and space, while in a doubly periodic model, the mean velocity varies only in the vertical and is constant in time, unless an explicit evolution equation for the mean state is included (e.g., Haidvogel and Held 1980; Vallis 1985, 1988; see discussion below).

The usefulness of a model of this type is supported by the results of Pavan and Held (1996). They show that, in a doubly periodic model, the PV fluxes produced as a function of the imposed mean shear are nearly the same as those produced at each latitude in an equilibrated channel model, for all but the narrowest baroclinic zones. In other words, given a local, steady-state mean shear (or equivalently, the local mean PV gradient) at a particular cross-channel location, and the local value of the mean PV flux, one arrives at the same relationship between flux and imposed gradients as in the horizontally homogeneous, doubly periodic model. Thus the fluxes produced by the baroclinic instability of a given mean state in a homogeneous model can be taken as a good approximation of those produced locally in an inhomogeneous flow that has the same local time-mean flow, as long as that mean flow is nearly constant over a few deformation radii horizontally.

The PV fluxes are a function of the local mean flow, but the zonal-mean steady state of the channel model is also a function of the PV fluxes. The steady state that evolves is one in which the tendency of eddies to flux PV down its mean gradient is balanced by the thermal relaxation of the zonal mean toward a baroclinically unstable state. In the spatially homogeneous model used for the present study, we implicitly assume that the mean state taken from hydrography results from a balance between large-scale thermal and wind forcing, which drive the mean state to be baroclinically unstable, and local eddy fluxes that act to remove mean PV gradients. This is sensible if large-scale forcing restores the mean faster than, or comparable to the rate at which eddies erode it. However, when the mean state is unstable at very small scales, this may not be a reasonable assumption.

The geostrophic mean shear computed from hydrography (the thin line in Fig. 6a) is an approximation of the true mean shear. This, due to the horizontal finite differences taken over the 0.5° GK04 grid, is less accurate than vertical profiles of N^2 (which themselves are of course not precise—see again the previous subsection). The mean QG PV gradient (2.3) is a function of

both $N^2(z)$ and $\mathbf{U}(z)$. Its profile, computed from hydrography, is plotted as the thin line in Fig. 6b. It reaches maximum values of more than 100β , which presumably reflect the inaccuracies in the computation from hydrography. As found in the linear calculation, these large PV gradients are confined to sharp, vertical regions and lead to fast growth at very small scales.

A simulation carried out with the fixed mean shear computed from hydrography results in a turbulent steady state with rms eddy velocities near 45 cm s^{-1} at the upper surface. This is about 3–4 times the observed surface eddy velocities (Stammer 1997; D. B. Chelton 2007, personal communication). One can assume that the excess eddy energy is due to either missing dissipation or excess generation, or a combination of both. We believe that the mean horizontal buoyancy gradients are noisy due to data sparsity, which, on differentiation, introduce much structure into the QGPV gradients on small vertical scales. In the simulation, the eddy PV flux generated by the hydrographic QGPV gradient can be huge but is directed systematically downgradient. Thus, if the mean flow is allowed to respond to the eddy fluxes on short time scales, this rich structure would be smoothed, leaving only large-scale features. We now devise a method to model the interaction of the PV flux with the mean flow.

c. A time-varying mean state

We allow the mean horizontal velocity to evolve in time by incorporating an eddy feedback:

$$\frac{\partial \mathbf{U}}{\partial t} = -\mathbf{z} \times \overline{\mathbf{u}'q'} - \tau_m^{-1}(\mathbf{U} - \mathbf{U}^{\text{target}}), \quad (3.1)$$

where $\mathbf{U} = \mathbf{U}(z, t)$ is the mean velocity, $\mathbf{U}^{\text{target}} = \mathbf{U}^{\text{target}}(z)$ is the target profile, computed via thermal wind balance from hydrography, τ_m is a restoring time, and $\overline{\mathbf{u}'q'}$ is the horizontally averaged horizontal eddy potential vorticity flux, computed at each time step in the computation. Note that there is no Coriolis term in (3.1) because the average is over both horizontal directions, and the turbulence is horizontally homogeneous. Vallis (1988) attempted a rigorous derivation of the equivalent of (3.1) for a two-layer model.⁴ Here we regard the closure statement (3.1) as an ad hoc representation that allows downgradient PV fluxes to quell the instability, acting against processes tending to restore the mean to an unstable state; the resulting mean is a balance between eddy-induced fluxes and the restoring.

The properties of the eddy feedback are as follows: in the horizontally homogeneous model, eddy relative vorticity fluxes vanish on horizontal averaging, and so

$$\overline{\mathbf{u}'q'} = f \frac{\partial}{\partial z} \left(\frac{\overline{\mathbf{u}'b'}}{B_z} \right). \quad (3.2)$$

Thus, if the buoyancy flux is downgradient, $\overline{\mathbf{u}'b'} = -\kappa_b \nabla B = f \kappa_b \mathbf{z} \times \mathbf{U}_z$ (where ∇B is the mean meridional buoyancy gradient and κ_b is an eddy buoyancy diffusivity), then the PV flux acts to vertically smooth the mean momentum (see, e.g., Greatbatch and Lamb 1990; Ferreira et al. 2005). The linear restoring force maintains the mean velocity close to its observed profile; taking a vertical derivative of (3.1) and applying thermal wind balance demonstrates that the restoring force maintains the mean available potential energy (APE), which is the source of the instability. Also note that since

$$\int_{-H}^0 \overline{\mathbf{u}'q'} dz = 0, \quad (3.3)$$

and assuming $\mathbf{U}(z, 0) = \mathbf{U}^{\text{target}}(z)$, the eddies only vertically redistribute horizontal momentum (the barotropic velocity does not change in time). Finally, dotting \mathbf{U} into (3.1) and integrating in z shows that a steady-state mean energy balance can be achieved between momentum dissipation and forcing by restoration.

The physical meaning of the time scale of the mean momentum restoration toward the target velocity can be understood as follows: To the extent that the eddy PV flux is locally proportional to the negative of the mean PV gradient (a good approximation, as will be discussed below), it will be strongest near the steepest features in the mean gradient. Therefore, the mean restoring force will only be effective at preserving the mean gradient against eddy fluxes that result from its larger-scale features—eddy fluxes with time scales slower than the restoring time τ_m . The small-scale features will be damped by the eddy flux. This approach is sensible if the large-scale features are set by the mean wind and buoyancy forcing on time scales on the order of the observed eddy time scale. Given that, for example, the mean current and eddy velocity scales in the ACC are roughly equivalent, this seems likely. Small-scale, rapidly growing eddies should be quite effective at attacking the mean gradients that generate them on time scales faster than the gradients can be restored by large-scale forcing. In this way, the eddy feedback mechanism enables one to proceed using noisy data, and results in a more robust calculation.

⁴ Further motivation for (3.1) comes from Eq. (2.50) of Wardle (2000): if ageostrophic and nonlinear terms are ignored and relaxation toward a mean velocity imposed, one has precisely (3.1).

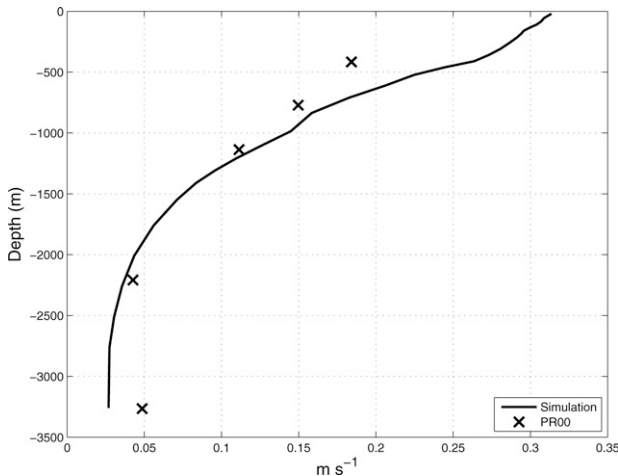


FIG. 8. The steady-state rms eddy velocity profile for the central simulation in which the mean state has been adjusted by eddy fluxes. Also shown are the measurements of eddy velocity scale (square root of the eddy kinetic energy) measured by PR00 (values shown are from their measurements in fixed coordinates).

A series of simulations was performed in which the restoring time was used as a control parameter. Once the time scale is shorter than the fastest linear growth rate (~ 5 days) by a factor of ~ 2 , the resulting steady-state mean flows become rather insensitive to further changes. Though the overall shear changes somewhat, the mean very quickly settles to a steady state in which all small-scale instabilities have been removed, as will be shown below.

The simulation we now discuss uses a short restoring time ($\tau_m = 0.4$) day to maintain the mean state close to the observed state. The resulting steady state velocity and PV gradient profiles are the thick black lines shown in Fig. 6. The mean velocity has, indeed, remained close to the initial state and, hence, close to the observed hydrography, and the mean kinetic energy (not shown) has been reduced by only about 10% from that of the initial profile. The apparent slight changes in the vertical structure of $\mathbf{s} \cdot \mathbf{U}$ however, are significant: the mean PV gradient has been dramatically reduced (thick line in the right of Fig. 6), and Fig. 8 (solid line) shows that the rms eddy velocity has been reduced to about 30 cm s^{-1} at the surface, much more in accord with observed values. Moreover, the steady-state eddy velocity profile is now very nearly equal to the square root of the eddy kinetic energies measured by PR00 (crosses in Fig. 8).

The structure developed in \mathbf{U} is, upon inspection, close to that of the mean buoyancy profile shown in Fig. 5. This occurs precisely because the PV flux is locally downgradient at all points in the vertical: the PV flux

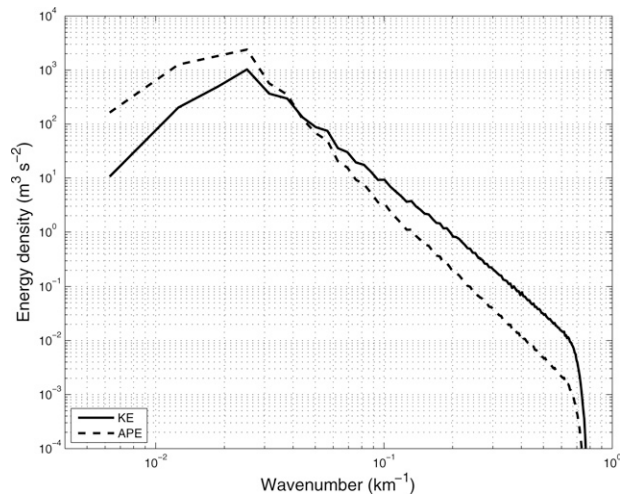


FIG. 9. The vertically and time-integrated eddy kinetic (solid line) and available potential (dashed line) energy spectra for the central simulation with a time-varying mean state.

works against the mean PV gradient, altering \mathbf{U} in such a way that the mean PV stretching term $(f\mathbf{z} \times \mathbf{U}_z/B_z)_z$ is reduced. The stretching term is reduced as the sharpest isopycnal slopes flatten, or equivalently as \mathbf{U}_z approaches to B_z . The stretching part of the steady-state mean PV gradient is thus reduced, and the structure of the instability accordingly changed. The dashed line in Fig. 7 shows the growth rate of the equilibrated mean state. Notably, the small-scale instabilities have been neutralized, while the largest-scale instability, due to a zero crossing of a first baroclinic mode component of the mean PV gradient, has remained intact. Note also that the neutralization occurs very quickly in the spin-down of the mean state.

To check that the mean eddy statistics are not affected by the time dependence of the mean state, we continued the run using the steady-state mean velocity $\langle \mathbf{U} \rangle(z)$ (the thick line in Fig. 6a; angle brackets denote a time average) fixed in time, and so not integrating (3.1). The resulting eddy fluxes (discussed in the next section), eddy scale, and eddy energy do not change, consistent with the results of Pavan and Held (1996).

The Doppler-shifted wave speeds found with the hydrographic and adjusted mean states indicate that, even though the instability has evolved, the steering level is even deeper, having moved from a depth of 900 to 1600 m. Spectra from the simulation (Fig. 9 shows the vertically integrated kinetic and available potential energy spectra) indicate a well-resolved enstrophy cascade and a typical eddy radius of about 40 km. The inverse cascade in this simulation is present but short: the eddies equilibrate at only about three times the deformation radius. Physical space fields (not shown) indicate that

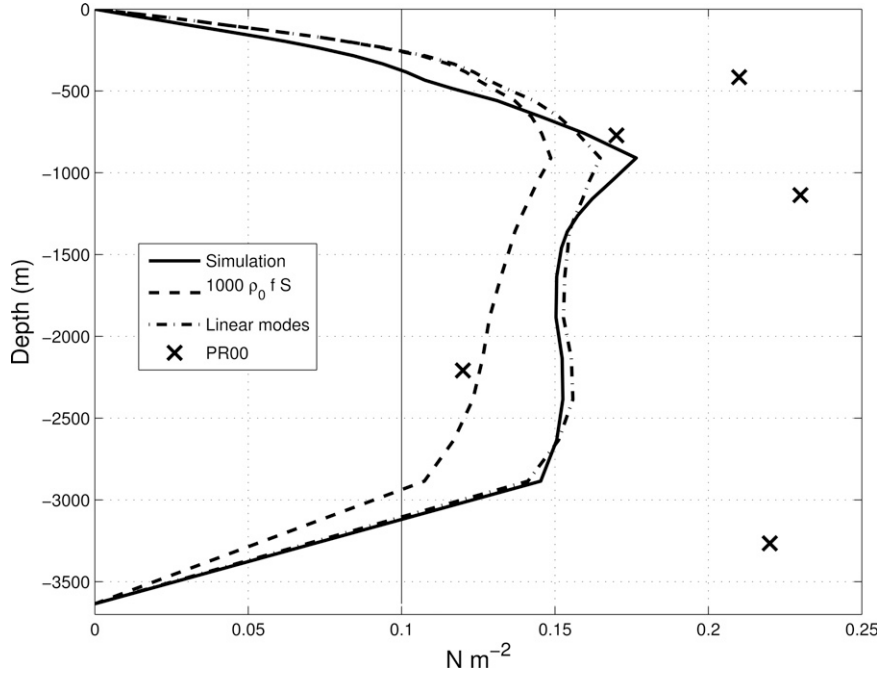


FIG. 10. The eddy stress (N m^{-2}) for the central simulation (solid line) and from the band-passed, shear-coordinate, South Station measurements of PR00 (crosses). Also plotted are estimates of eddy stress using the second term in (4.2) with a constant diffusivity $\kappa_b = 1000 \text{ m}^2 \text{ s}^{-1}$ (dashed line) as well as an estimate using the fastest-growing linear mode (dashed-dotted line). The thin vertical line indicates a typical value of the surface wind stress.

the flow is horizontally homogeneous—no jets form—consistent with a drag-based cascade-halting mechanism (Smith et al. 2002).

4. Simulated versus observed eddy stress and diffusivity

The usefulness of this type of process model is as a tool by which to measure the eddy statistics and fluxes that result from the local instability of the mean state. Here we review some fundamentals of eddy-driven circulation and compare our results from the equilibrated model state with the measurements of PR00.

a. Eddy form stress

Eddies influence the interior circulation of the ACC through form stress, which transfers horizontal momentum vertically. This is most apparent in the residual mean framework, as discussed in Marshall and Radko (2003) and Ferreira et al. (2005). Summarizing, the steady-state, mean cross-stream momentum equation in residual form is

$$-f \mathbf{n} \cdot \bar{\mathbf{u}}_{\text{res}} = \frac{1}{\rho_0} \frac{\partial \tau_{\text{wind}}^s}{\partial z} + \mathbf{n} \cdot \overline{\mathbf{u}'q'}, \quad (4.1)$$

where τ_{wind}^s is the along-stream wind stress at the surface and $\mathbf{n} \cdot \bar{\mathbf{u}}_{\text{res}} = \mathbf{n} \cdot [\bar{\mathbf{u}} - \partial_z (\overline{\mathbf{u}'b'}/B_z)]$ is the residual mean cross-stream velocity. The cross-stream PV flux can be expressed as the vertical divergence of an eddy stress, neglecting the contribution of horizontal eddy momentum fluxes (which are small in the ocean and by construction vanish in our model):

$$\mathbf{n} \cdot \overline{\mathbf{u}'q'} = \frac{1}{\rho_0} \frac{\partial \tau_{\text{eddy}}^s}{\partial z},$$

where

$$\tau_{\text{eddy}}^s = \rho_0 f \frac{\mathbf{n} \cdot \overline{\mathbf{u}'b'}}{B_z} = \rho_0 f \kappa_b \mathbf{n} \cdot \mathbf{S} \quad (4.2)$$

is the interfacial form stress; κ_b is an eddy buoyancy diffusivity defined by the relation $\overline{\mathbf{u}'b'} = -\kappa_b \nabla B$. This is essentially (3.2) applied to the residual mean framework.

Observed estimates of the eddy form stress (4.2) at the target location are plotted in Fig. 10. The simulated result (the solid line) indicates that the peak stress is near the 1-km depth found in the linear and observational analyses, but it is significant over depths ranging from 1 to 3 km. Also shown are two intermediate estimates: the second term in (4.2) assuming a constant

diffusivity $\kappa_b = 1000 \text{ m}^2 \text{ s}^{-1}$ (dashed line) and an estimate made by integrating the linear normal-mode approximation for the PV flux (2.4) up from the bottom and using the relation (3.2) (dashed-dotted line). (Note, however, that the linear estimate was adjusted with a nondimensional constant to give the displayed result.) The constant diffusivity estimate provides a useful reference. While the estimate itself is not very accurate, with a constant diffusivity it reflects exactly the shape of the isopycnal slope \mathbf{S} . Thus, the peak at 1 km reflects a peak in isopycnal slope at that depth.

The stress values from PR00 (crosses in Fig. 10) are taken from their analysis of the South Station mooring of the Australian Subantarctic Front (AUSSAF) array (the South Station data was chosen because it exhibited the highest statistical significance for eddy heat flux). The plotted values represent their band-passed data (40 h to 90 days) in shear coordinates—a coordinate frame adjusted daily to account for changes in the position of the mean jet. The measured values are close in magnitude to the simulated and estimated values ($0.1\text{--}0.2 \text{ N m}^{-2}$) and consistent with a presumed balance between eddy stress and surface wind stress (Johnson and Bryden 1989). However, the vertical structure is erratic, and the overall stress is larger. The data suffers from three unavoidable factors that may diminish its accuracy: (i) rotational fluxes (see, e.g., Marshall and Shutts 1981) are not removed, (ii) the length of the time series may be shorter than necessary to have well-converged eddy statistics, and (iii) only the temperature field is considered—salinity effects on buoyancy are necessarily neglected. The model results, on the other hand, suffer from the assumptions of quasigeostrophic dynamics and of horizontally homogeneous statistics. Despite uncertainties in each approach, the values are close enough to argue that the simulated results present a useful estimate of the measured vertical structure of eddy fluxes.

b. Eddy fluxes and diffusivities of PV and buoyancy

Taking the model output as a proxy for the actual eddy fluxes, we consider further the implied diffusivities of PV and buoyancy. A common and useful assumption is that eddy fluxes result from a downgradient transfer process. Moreover, as it is PV that is materially conserved, it makes dynamical sense to think of PV as being the diffused quantity. Does this make any difference in the absence of momentum fluxes and, as is the case here, with β effectively small? In this section we investigate eddy fluxes and diffusivities for both buoyancy and PV, as well as for a true tracer.

Figure 11 shows the horizontally averaged PV (Fig. 11a, solid line) and buoyancy (Fig. 11b, solid line) fluxes, along with the simple estimates $-1000 \mathbf{n} \cdot \nabla Q$ and $-1000 \mathbf{n} \cdot \nabla B$, respectively (dashed lines). For comparison with the observations of Gille (2003), we note that a cross-stream buoyancy flux of $0.5 \times 10^{-5} \text{ m}^2 \text{ s}^{-3}$ is equivalent to a heat flux of 10 kW m^{-2} , assuming $C_p = 4000 \text{ J Kg}^{-1} \text{ K}^{-1}$ and a thermal expansion coefficient for water of $2 \times 10^{-4} \text{ K}^{-1}$. Gille (2003) finds typical heat fluxes of order 7 kW m^{-2} at a depth of 900 m, or roughly half of the equivalent typical flux we find in Fig. 11b. Of course, for the same reasons discussed at the end of the previous section, one should not expect an exact correspondence between the simulated results and observations. Moreover, the data of Gille (2003) represent an average over the circumpolar region.

Figure 11 shows that eddies flux PV and buoyancy down their respective mean gradients, and do so nearly locally with depth. However, we will see that the diffusivities for PV and buoyancy are different from one another and show strong depth dependence. As is well known, writing $\overline{\mathbf{u}'q'} = -\kappa_q \nabla Q$ with κ_q a constant violates the kinematic requirement (3.3): if β is not negligible, then $\int \nabla Q dz \neq 0$ (the stretching part of the mean PV gradient itself does integrate to zero, if the mean flow satisfies the same boundary conditions as the eddies). Therefore, κ_q must be a function of depth. Indeed, this constraint was used by Marshall (1981) to help guide the choice of vertical variation of the diffusivity in a zonal-average model of the ACC. Moreover, in baroclinically unstable flow, ∇Q must vanish somewhere in the domain, making κ_q difficult to diagnose from knowledge of the eddy PV flux and the mean PV gradient. Defining a buoyancy diffusivity as below (4.2), on the other hand, poses no problems, as ∇B need not be zero anywhere (and in the present case, it is not). Nevertheless, we shall see that the PV dynamics controls the eddies and best characterizes the mixing in the fluid.

The diffusivities for PV (κ_q , solid line) and buoyancy (κ_b , dashed line) from the simulation are plotted in Fig. 12, along with the estimate $\kappa_{q,\text{lin}}$ (dotted line with squares) from the linear theory (2.4), the estimate $\kappa_{\text{eddy}} = 0.5V_{\text{eddy}} L_{\text{eddy}}$ (dotted line with circles, discussed below), measurements of the eddy temperature diffusivity by H. E. Phillips and S. R. Rintoul (2007, personal communication; crosses in Fig. 12) and the “effective diffusivity” of an ideal tracer (dashed-dotted line, discussed below). The PV and buoyancy diffusivities are computed directly from the flux-gradient relationship (note that in the calculation of κ_q , wher-

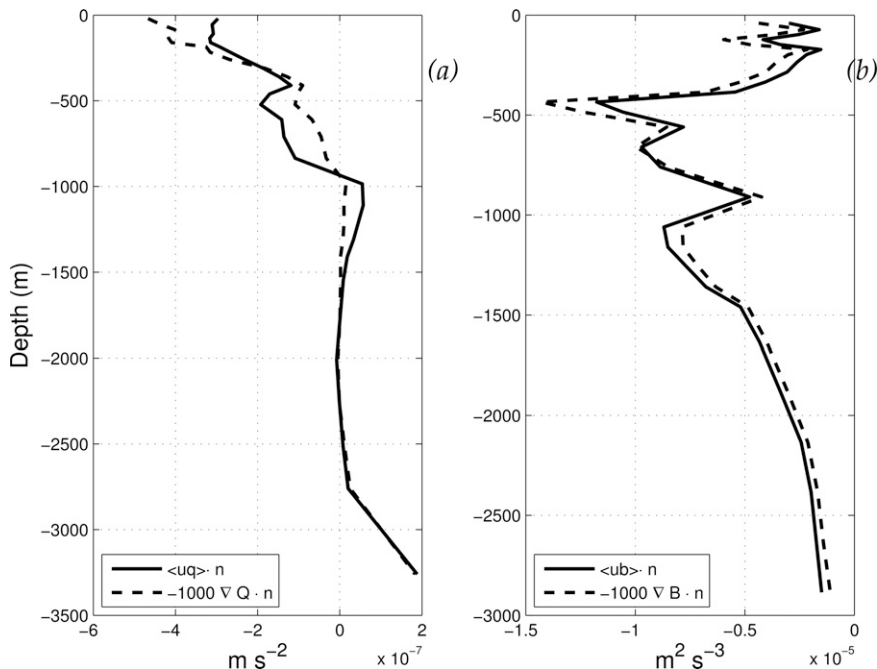


FIG. 11. (a) Horizontal and time average of steady-state cross-stream QGPV flux $\langle \mathbf{u}'q' \rangle \cdot \mathbf{n}$ (solid line) and (b) the average cross-stream eddy buoyancy flux $\langle \mathbf{u}'b' \rangle \cdot \mathbf{n}$ (solid line). Note that as discussed in the text, a buoyancy flux of $0.5 \times 10^{-5} \text{ m}^2 \text{ s}^{-3}$ corresponds to a heat flux of 10 kW m^{-2} . The dashed lines are estimates of the former averages obtained by assuming a constant downgradient diffusion with diffusivity $1000 \text{ m}^2 \text{ s}^{-1}$ for each (dashed lines).

ever ∇Q is less than a threshold value of $\beta/10$, neighboring values of κ_q are averaged—only one point, near $z = -1200 \text{ m}$, required this correction). The results for the various diffusivities are strikingly different in structure and magnitude, particularly between κ_q and κ_b . The buoyancy diffusivity κ_b varies rather smoothly from about 600 near the surface to $1500 \text{ m}^2 \text{ s}^{-1}$ at the bottom. The PV diffusivity κ_q , on the other hand, is sharply peaked just below 1-km depth, reaching values of over $5000 \text{ m}^2 \text{ s}^{-1}$ with values less than $1000 \text{ m}^2 \text{ s}^{-1}$ at the top and bottom (the dashed-dotted line is discussed in the next subsection).

The linear estimate $\kappa_{q,\text{lin}}$ is computed using the same multiplicative constant used for the linear eddy stress estimate plotted in Fig. 10. The linear diffusivity estimate is peaked at middepth as expected, but its peak is lower down than for κ_q , and its overall structure does not accurately reflect the simulated structure. It nevertheless does reflect the prominence of eddy mixing at depth.

The mixing-length estimate $\kappa_{\text{eddy}} = 0.5V_{\text{eddy}} L_{\text{eddy}}$ is computed using the eddy velocity V_{eddy} , shown in Fig. 8, and an eddy-scale estimate L_{eddy} taken as the inverse centroid of the kinetic energy spectrum at each depth. The factor 0.5 is chosen somewhat arbitrarily to fit the results in scale to those in the figure. This estimate is

largest at the surface (just like the effective diffusivity estimate, discussed below) but fails to show the peak that is apparent in the PV diffusivity. The structure comes from the fact that the eddies are near barotropic and thus have the same scale at all depths. The resulting diffusivity estimate thus bears the structure of the eddy velocity, which is peaked near the surface. This is discussed further below.

The diffusivity values computed by PR00 are computed by dividing the cross-stream eddy temperature flux by minus the mean temperature gradient and, so, actually represent a temperature diffusivity κ_T . The values plotted in Fig. 10 are taken from their South Station, band-passed, shear-coordinate measurements, consistent with the measured stress values from their analysis. We reiterate here that the computation of stress and diffusivity from PR00 as well as of mean gradients, neglects salinity effects and does not remove rotational fluxes; therefore, the measured temperature diffusivity should not be expected to exactly match the simulated buoyancy diffusivity.

One might wonder whether the simulated diffusivities κ_q and κ_b can possibly be consistent with one another, given their enormous difference in magnitude and structure. In quasigeostrophic theory, the horizontally averaged eddy buoyancy and PV fluxes are related

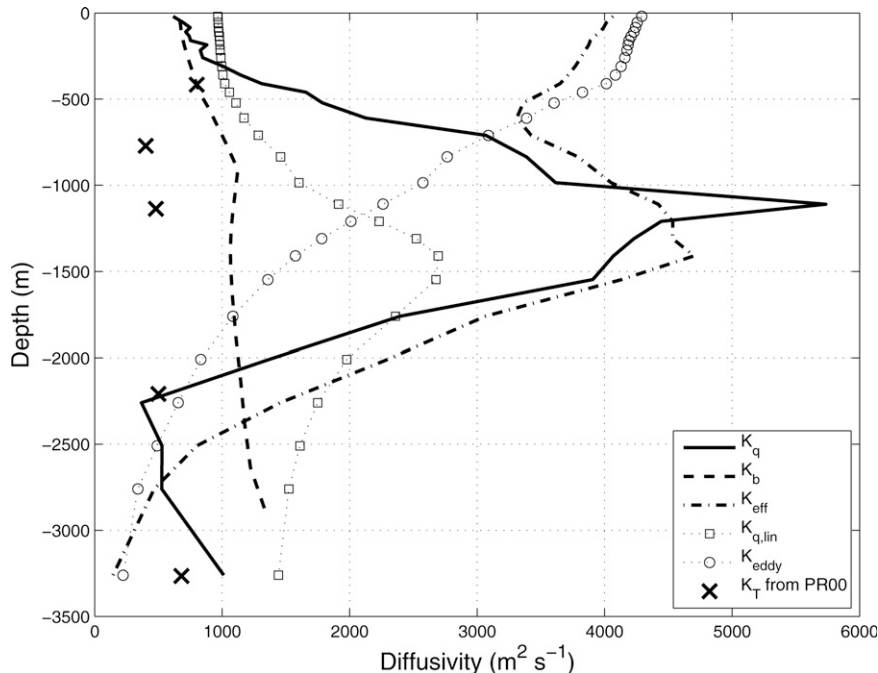


FIG. 12. Simulated, estimated, and measured diffusivities ($\text{m}^2 \text{s}^{-1}$). QGPV diffusivity (κ_q , solid line) and buoyancy diffusivity (κ_b , dashed line) were computed by dividing cross-stream eddy fluxes by the negative of their cross-stream mean gradients (both plotted in Fig. 11). Where the QGPV mean gradient is less than $\beta/10$, κ_q is computed by taking a weighted average of values above and below that level. The dashed-dotted line is the effective diffusivity κ_{eff} of the flow computed by transforming an advected tracer into area coordinates (see text for details). The dotted line with squares is the estimate from (2.4), using the same multiplicative factor as used in the linear eddy stress estimate in Fig. 10. The dotted line with circles is an eddy mixing-length estimate, computed as $K_{\text{eddy}} = 0.5V_{\text{eddy}} L_{\text{eddy}}$, where V_{eddy} is shown in Fig. 8, and L_{eddy} is an estimate of the eddy length scale from the kinetic energy spectrum (Fig. 9). The crosses are band-passed, shear-coordinate estimates from the South Station measurements of PR00 (consistent with the PR00 stress measurements shown in Fig. 10).

as in (3.2) (recall that a horizontal average is denoted by an overbar and that relative vorticity fluxes vanish in this average for homogeneous statistics). Using the relationship between PV and buoyancy fluxes (2.3) and thermal wind balance yields the relation

$$\kappa_q \left(\frac{\partial \mathbf{S}}{\partial z} - \frac{\beta}{f} \mathbf{y} \right) = \frac{\partial}{\partial z} (\kappa_b \mathbf{S}). \quad (4.3)$$

If β is negligible, then a constant κ_b and constant κ_q can be consistent (though they need not be); otherwise, constant diffusivities cannot be consistent with one another. The lhs and rhs of (4.3) (dotted into \mathbf{S}) are plotted in Fig. 13, showing that the two diffusivity functions are, indeed, consistent with one another. The dashed-dotted line shows the lhs of (4.3) without the β term—the deviation of this curve from the other two clearly shows that β is not negligible, so PV and buoyancy diffusion cannot be approximated as equal to one another.

c. The effective diffusivity

Given such a large difference between PV and buoyancy diffusion, how will a truly passive tracer be mixed? We address this question by computing the effective diffusivity of the simulated flow. The effective diffusivity, pioneered by Nakamura (1996) (see also Shuckburgh and Haynes 2003; Marshall et al. 2006), is a diagnostic measure of the enhancement of mixing in high-Peclet number flows by the advective stretching and folding of tracer contours. It is an intrinsic measure of the mixing ability of the flow itself, independent of the tracer.

The effective diffusivity for the simulation discussed above is computed as follows: a passive tracer is added to the steady-state flow at each vertical level, obeying the advection-diffusion equation

$$\frac{\partial C}{\partial t} + (\mathbf{u}' + \langle \mathbf{U} \rangle) \cdot \nabla_H C = \kappa \nabla_H^2 C,$$

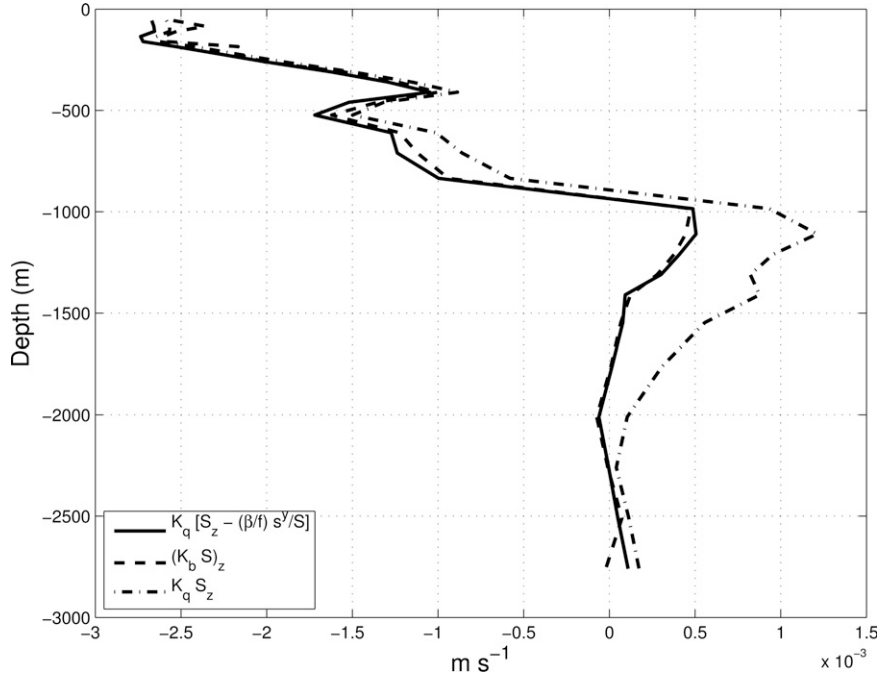


FIG. 13. Test of consistency of κ_q and κ_b with one another and assessment of the effects of β on the diffusivities. The solid line is the left-hand side of (4.3) and the dashed line is the right-hand side of that equation. The dashed-dotted line is the left-hand side of (4.3) with β set to 0.

where, during this computation, the mean velocity is held to its steady value $\langle \mathbf{U} \rangle$ (recall that the energy and scale of the flow do not change after the mean velocity has adjusted to a steady state). Two different initial conditions were used: the first was a sinusoidal profile,

$$C(x, y, z, t = 0) = \sin\left(\frac{2\pi y}{L}\right) - \frac{1}{2},$$

where L is the horizontal domain extent and ∇_H is the horizontal gradient operator. The second is based on the mean PV gradient so as to make the tracer as much like the PV field as possible. Specifically, we let $C(x, y, z, t = 0) = G(z)y$, where $G(z) = \mathbf{n} \cdot \nabla Q$ (i.e., the cross-stream mean PV gradient rotated to the y direction, because the mean does not rotate with depth and the flow is isotropic) and make the substitution $C = G(\phi + y)$, where $\phi = \phi(x, y, z, t)$ solves

$$\frac{\partial \phi}{\partial t} + (\mathbf{u}' + \langle \mathbf{U} \rangle) \cdot \nabla_H \phi + v' + \langle V \rangle = \kappa \nabla_H^2 \phi,$$

with $\phi(x, y, z, t = 0) = 0$. The tracer ϕ is simulated, and the tracer C is reconstructed from ϕ .

In both cases, the tracer is diffused horizontally with coefficient $\kappa = 42 \text{ m}^2 \text{ s}^{-1}$ —this value ensures that the Batchelor scale $\sqrt{\kappa/\sigma}$ is resolved (σ is the horizontal

strain rate, computed for the steady state). At each time and vertical level, the tracer field is converted to area coordinates $\mathcal{A} = \mathcal{A}(C)$, and the squared equivalent length (see Shuckburgh and Haynes 2003)

$$L_{\text{eq}}^2 = L_{\text{eq}}^2(\mathcal{A}) = \frac{1}{(\partial C / \partial \mathcal{A})^2} \frac{\partial}{\partial \mathcal{A}} \int_{\mathcal{A}} |\nabla C|^2 d\mathcal{A}$$

is calculated for a discrete range of 100 tracer values between the maximum $1/2$ and minimum $-1/2$. Laplacian diffusion erodes the maxima and minima slightly, but for all tracer contour values near the middle of the range, the equivalent length rather quickly settles to a steady-state value, reflecting a balance between stirring and mixing. From the steady-state range and central tracer contour values, a mean is taken (denoted by angle brackets); this value is used to compute the effective diffusivity via

$$\kappa_{\text{eff}} = \kappa \left(\frac{\langle L_{\text{eq}} \rangle}{L_{\text{min}}} \right)^2,$$

where L_{min} is the minimum tracer contour length—with the sinusoidal initial condition used here, $L_{\text{min}} = 2$.

Remarkably, both initial conditions (one with knowledge of the mean PV gradient, the other without) produce nearly identical profiles of effective diffusivity.

The diffusivity resulting from the initial condition based on the mean PV gradient is plotted as the dashed-dotted line in Fig. 12 (resulting from the sinusoidal initial condition is not shown). Apparently potential vorticity is diffused very much like the passive tracer at depth, but less so near the surface. On the other hand, the mixing length estimate κ_{eddy} is similar to the effective diffusivity near the surface, but not at depth. One possible explanation for the difference at the surface is that the PV mixing is suppressed there since the mean PV gradient is largest at the surface. The effective diffusivity, on the other hand, results in part from the energy of the flow, which is largest at the surface. The effective diffusivity is also large between 1000 and 1500 m depth, where the PV diffusivity has its peak. Here the mean PV gradient is near zero, which is the cause of the main instability generating the mixing, and both the tracer and PV respond. This is a speculative explanation; more locations will be studied in future work to pin down the generic behavior of the diffusivities.

Overall, the results indicate that (i) PV and buoyancy are not mixed in the same way, (ii) the mixing of PV and tracers is similar at depth but differs near the surface and (iii) both tracer and PV mixing are enhanced near a depth of 1 km, as originally suggested by surface signals that indicate a steering level at this depth.

5. Discussion and conclusions

Encouraged by the observation that the steering level of baroclinic waves in the ACC is at significant depth, we have carried out a detailed stability analysis of the hydrographic structure of the Southern Ocean. The steering level of the fastest growing linear mode is, indeed, found to be consistently at a depth of 1 to 1.5 km in the region of circumpolar flow around Antarctica.

We proceeded to study the stability properties of one particular region of the Southern Ocean, corresponding to the in situ observations from the mooring array of PR00. Using a fully nonlinear, doubly periodic quasi-geostrophic model, configured in such a way that the eddies spawned by it could interact with the mean flow, we studied the vertical structure of the resulting eddies and eddy fluxes. We found that

- computed eddy fluxes and statistics are broadly consistent with the observations of Phillips and Rintoul (2000);
- the steering level is at about 1-km depth in the water column, in accord with our inference from altimetric observations;

- eddy diffusivities for potential vorticity (κ_q) and tracers (κ_{eff}) are rather similar to one another both in structure and magnitude: they have a marked vertical structure and exhibit a significant peak at the steering level where the diffusivity reaches a magnitude of about $5000 \text{ m}^2 \text{ s}^{-1}$; the linear prediction (2.4) for the PV diffusivity captures some features of the simulated vertical structure of κ_q , but not, of course, its magnitude;
- the eddy diffusivity for buoyancy κ_b does not exhibit intense vertical structure and has a magnitude of about $1000 \text{ m}^2 \text{ s}^{-1}$, significantly smaller than the PV and tracer diffusivities;
- the eddy stress has a relatively simple vertical structure, increasing from zero at the surface to reach a maximum value (on the order of the surface wind stress) at the steering level before decaying again to zero at depth.

We now conclude by discussing the implications of these results for (i) the parameterization of eddies and stirring in large-scale models and (ii) the dynamics of the ACC and its overturning circulation.

a. Implications for mixing and parameterization

The results presented here have important implications for the parameterization of eddies in large-scale models, as summarized in Fig. 12. Current eddy parameterization schemes derive from the work of Gent and McWilliams (1990) and comprise two parts:

- (i) the skew component of the eddy buoyancy flux (i.e., that which is directed along buoyancy surfaces) is represented as an advective process and involves the parameterization of the horizontal component of the eddy buoyancy flux, $\overline{\mathbf{u}'b'}$, which is assumed to be fluxed down the horizontal buoyancy gradient, namely, $\overline{\mathbf{u}'b'} = -\kappa_b \nabla_H B$; the diffusivity κ_b is more often than not assumed to be constant in space (but see Danabasoglu and McWilliams 1995; Visbeck et al. 1997; Ferreira et al. 2005); and
- (ii) tracer gradients along buoyancy surfaces are mixed at a rate assumed to be the same as κ_b .

Our study lends support to elements of Gent and McWilliams (1990). For example, as shown in Fig. 10, setting κ_b to a constant value of $1000 \text{ m}^2 \text{ s}^{-1}$, one can reconstruct the broad features of the vertical variations of the eddy stress, a key target of any parameterization. However, (i) the lack of structure found in κ_b at the target location studied here may not be a generic feature of eddy flows and (ii), while it is generally assumed

that tracers are stirred along buoyancy surfaces with the same diffusivity as buoyancy, this may be inappropriate because here we find that κ_{eff} is 5 times larger than κ_b .

One way forward is to adopt a residual mean perspective (Ferreira and Marshall 2006) and parameterize the eddy potential vorticity flux as a downgradient process with eddy diffusivity κ_q and mix tracers along buoyancy surfaces at the same rate. The degree to which one can make use of linear theory to guide in the prescription of the vertical variation of κ_q , as argued by Green (1970) and Killworth (1997), will be the focus of a future publication.

b. Implications for ACC dynamics

Tracer distributions in the Southern Ocean depend on both the magnitude and direction of the residual flow and the vigor by which they are stirred by meso-scale eddies. The residual circulation is given by, to the extent that streamwise-average theory is appropriate, the streamwise residual momentum equation (4.1) (neglecting Reynold stresses), which is equivalent to (integrating vertically and applying boundary conditions that $\Psi_{\text{res}} = \tau_{\text{eddy}}^s = 0$ at the top)

$$\rho_0 f \Psi_{\text{res}} = -\tau_{\text{wind}}^s + \tau_{\text{eddy}}^s$$

as in, for example, Marshall and Radko (2003). In illustration, Fig. 10 shows our predictions of $\tau_{\text{eddy}}^s(z)$.

The sense of the implied residual circulation can be understood by considering the PV flux itself. Assuming that the wind stress only penetrates the upper ocean, (4.1) indicates that the residual velocity will be determined by the PV flux in the interior (keep in mind that $f < 0$). Figure 11a plots $\mathbf{n} \cdot \overline{\mathbf{u}'\mathbf{q}'}$ as a function of depth. We see that v_{res} is directed poleward in the upper part of the water column and equatorward beneath. This is in the sense to flatten isopycnals, as is to be expected since the eddies are obtaining their energy from the mean APE. The eastward-directed wind stress balances the process, acting to tilt up the isopycnals and restore the APE.

We note that the eddy stress τ_{eddy}^s in Fig. 10 is of the same magnitude as the wind stress, typically about 0.1 N m^{-2} , as marked with a straight line. If τ_{eddy}^s exactly balances τ_{wind}^s , then we have the limit of vanishing residual mean circulation suggested by Johnson and Bryden (1989). This balance is not expected to hold at every point but rather only in an integral sense. The local difference between τ_{eddy}^s and τ_{wind}^s supports a non-zero residual flow.

The residual flow is sensitive to the vertical structure of τ_{eddy}^s , which tends to peak at the steering level (where ∇Q changes sign). In the core of the ACC, the steering level is rather deep in the water column, consistent with a first baroclinic mode structure for a deep pycnocline. However, according to our linear analysis, we see in Fig. 4a that the steering level rises toward the surface on the equatorial flank of the ACC, so one might expect the peak in the eddy stress and diffusivity term to follow that pattern, resulting in a residual flow that exhibits much structure near the surface. The generally shallow steering level away from the axis of the ACC might account for the benefit observed in global ocean models of using a diffusivity that is enhanced near the surface (Ferreira et al. 2005; Danabasoglu and Marshall 2007). Finally, the sense of the residual meridional turning circulation is of great importance and debate. The ‘‘diabatic Deacon cell’’ described in Speer et al. (2000) has equatorward flow in the upper part of the water column, presumably a direct consequence of driving by the wind. Lower down in the water column there is poleward flow. The Marshall and Radko (2003, 2006) model of the upper cell has the same general form. The sense of the residual flow driven by eddies, implied by Fig. 11, is poleward above 1 km and equatorward below. The ageostrophic flow associated with the wind (not plotted in Fig. 11) will also be directed equatorward. The deeper equatorward flow may be capturing part of the deep overturning cell, which has the opposite sign to the upper cell—see Fig. 1 of Marshall and Radko (2006). However, it is important to remember that it is not possible to extrapolate from one vertical profile of cross-stream eddy PV flux or stress. It is necessary to repeat our calculations at many points in the Southern Ocean to build a climatology. Such calculations are ongoing.

Acknowledgments. The authors thank Helen Hill for a great deal of help with the figures and analysis, Chris Hughes for use of his altimetric phase speed analysis, Nikolai Maximenko for use of his surface drifter data, and Geoff Vallis for discussions and advice. JM acknowledges the support of the Polar Programs Division of NSF; KSS acknowledges the support of NSF Grant OCE0327470. Both authors acknowledge the support of the GFD program, sponsored by NSF OCE.

REFERENCES

Arbic, B. K., and R. B. Scott, 2008: On quadratic bottom drag, geostrophic turbulence, and oceanic mesoscale eddies. *J. Phys. Oceanogr.*, **38**, 84–103.

- Bauer, S., M. S. Swenson, and A. Griffa, 2002: Eddy mean flow decomposition and eddy diffusivity estimates in the tropical Pacific Ocean: 2. Results. *J. Geophys. Res.*, **107**, 3154, doi:10.1029/2000JC000613.
- Chelton, D. B., and M. G. Schlax, 1996: Global observations of oceanic Rossby waves. *Science*, **272**, 234–238.
- , —, R. M. Samelson, and R. A. de Szoeke, 2007: Global observations of large oceanic eddies. *Geophys. Res. Lett.*, **34**, L15606, doi:10.1029/2007GL030812.
- Danabasoglu, G., and J. McWilliams, 1995: Sensitivity of the global ocean circulation to parameterizations of mesoscale tracer transports. *J. Climate*, **8**, 2967–2987.
- , and J. Marshall, 2007: Effects of vertical variations of thickness diffusivity in an ocean general circulation model. *Ocean Modell.*, **18**, 122–141.
- Ferreira, D., and J. Marshall, 2006: Formulation and implementation of a residual mean ocean circulation model. *Ocean Modell.*, **13**, 86–107.
- , —, and P. Heimbach, 2005: Estimating eddy stresses by fitting dynamics to observations using a residual mean ocean circulation model and its adjoint. *J. Phys. Oceanogr.*, **35**, 1891–1910.
- Gent, P. R., and J. C. McWilliams, 1990: Isopycnal mixing in ocean circulation models. *J. Phys. Oceanogr.*, **20**, 150–155.
- Gill, A. E., J. S. A. Green, and A. J. Simmons, 1974: Energy partition in the large-scale ocean circulation and the production of midocean eddies. *Deep-Sea Res.*, **21**, 499–528.
- Gille, S., 2003: Float observations of the Southern Ocean. Part II: Eddy fluxes. *J. Phys. Oceanogr.*, **33**, 1182–1196.
- Gouretski, V. V., and K. P. Koltermann, 2004: WOCE global hydrographic climatology, a technical report. Berichte des Bundesamtes für Seeschifffahrt und Hydrographie Tech. Rep. 35, 52 pp.
- Greatbatch, R. J., and K. G. Lamb, 1990: On parameterizing vertical mixing of momentum in non-eddy resolving ocean models. *J. Phys. Oceanogr.*, **20**, 1634–1637.
- Green, J. S. A., 1970: Transfer properties of the large-scale eddies and the general circulation of the atmosphere. *Quart. J. Roy. Meteor. Soc.*, **96**, 157–185.
- Griani, N., I. M. Held, K. S. Smith, and G. K. Vallis, 2004: The effects of quadratic drag on the inverse cascade of two-dimensional turbulence. *Phys. Fluids*, **16**, 1–16.
- Haidvogel, D. B., and I. M. Held, 1980: Homogeneous quasigeostrophic turbulence driven by a uniform temperature gradient. *J. Atmos. Sci.*, **37**, 2644–2660.
- Holloway, G., 1986: Eddies, waves, circulation, and mixing: Statistical geofluid mechanics. *Annu. Rev. Fluid Mech.*, **18**, 91–147.
- Howard, L. N., 1961: Note on a paper of John Miles. *J. Fluid Mech.*, **10**, 509–512.
- Hughes, C. W., 1996: The Antarctic Circumpolar Current as a waveguide for Rossby waves. *J. Phys. Oceanogr.*, **26**, 1375–1387.
- Jackett, D. R., and T. J. McDougall, 1997: A neutral density variable for the world's oceans. *J. Phys. Oceanogr.*, **27**, 237–263.
- Johnson, G. C., and H. L. Bryden, 1989: On the size of the Antarctic Circumpolar Current. *Deep-Sea Res.*, **36**, 39–53.
- Karsten, R. H., and J. C. Marshall, 2002: Constructing the residual circulation of the ACC from observations. *J. Phys. Oceanogr.*, **32**, 3315–3327.
- Killworth, P. D., 1997: On the parameterization of eddy transfer. Part I: Theory. *J. Mar. Res.*, **55**, 1171–1197.
- , and J. R. Blundell, 2007: Planetary wave response to surface forcing and to instability in the presence of mean flow and topography. *J. Phys. Oceanogr.*, **37**, 1297–1320.
- Lozier, M. S., and D. Bercovici, 1992: Particle exchange in an unstable jet. *J. Phys. Oceanogr.*, **22**, 1506–1516.
- Marshall, J. C., 1981: On the parameterization of geostrophic eddies in the ocean. *J. Phys. Oceanogr.*, **11**, 1257–1271.
- , and G. Shutts, 1981: A note on rotational and divergent eddy fluxes. *J. Phys. Oceanogr.*, **11**, 1677–1680.
- , and T. Radko, 2003: Residual mean solutions for the Antarctic Circumpolar Current and its associated overturning circulation. *J. Phys. Oceanogr.*, **33**, 2341–2354.
- , and —, 2006: A model of the upper branch of the meridional overturning circulation of the Southern Ocean. *Prog. Oceanogr.*, **70**, 331–345.
- , D. Olbers, D. Wolf-Gladrow, and H. Ross, 1993: Potential vorticity constraints on the hydrography and transport of the Southern Ocean. *J. Phys. Oceanogr.*, **23**, 465–487.
- , E. Shuckburgh, H. Jones, and C. Hill, 2006: Estimates and implications of surface eddy diffusivity in the Southern Ocean derived from tracer transport. *J. Phys. Oceanogr.*, **36**, 1806–1821.
- Meinen, C. S., and D. S. Luther, 2003: Comparison of methods of estimating mean synoptic current structure in “stream coordinate” reference frames with an example from the Antarctic Circumpolar Current. *Deep-Sea Res.*, **50**, 201–220.
- Nakamura, N., 1996: Two-dimensional mixing, edge formation, and permeability diagnosed in area coordinates. *J. Atmos. Sci.*, **53**, 1524–1537.
- Pavan, V., and I. M. Held, 1996: The diffusive approximation for eddy fluxes in baroclinically unstable jets. *J. Atmos. Sci.*, **53**, 1262–1272.
- Pedlosky, J., 1984: The equations for geostrophic motion in the ocean. *J. Phys. Oceanogr.*, **14**, 448–455.
- Phillips, H. E., and S. R. Rintoul, 2000: Eddy variability and energetics from direct current measurements in the Antarctic Circumpolar Current south of Australia. *J. Phys. Oceanogr.*, **30**, 3050–3076.
- Robinson, A., and J. McWilliams, 1974: The baroclinic instability of the open ocean. *J. Phys. Oceanogr.*, **4**, 281–294.
- Scott, R. B., and F. Wang, 2005: Direct evidence of an oceanic inverse kinetic energy cascade from satellite altimetry. *J. Phys. Oceanogr.*, **35**, 1650–1666.
- Shuckburgh, E. F., and P. H. Haynes, 2003: Diagnosing tracer transport and mixing using a tracer-based coordinate system. *Phys. Fluids*, **15**, 3342–3357.
- Smith, K. S., 2007: The geography of linear baroclinic instability in Earth's oceans. *J. Mar. Res.*, **65**, 655–683.
- , and G. K. Vallis, 2002: The scales and equilibration of mid-ocean eddies: Forced dissipative flow. *J. Phys. Oceanogr.*, **32**, 1699–1721.
- , G. Boccaletti, C. C. Henning, I. N. Marinov, C. Y. Tam, I. M. Held, and G. K. Vallis, 2002: Turbulent diffusion in the geostrophic inverse cascade. *J. Fluid Mech.*, **469**, 13–48.
- Smith, W. H. F., and D. T. Sandwell, 1997: Global seafloor topography from satellite altimetry and ship depth soundings. *Science*, **277**, 1957–1962.

- Speer, K., S. R. Rintoul, and B. Sloyan, 2000: The diabatic Deacon cell. *J. Phys. Oceanogr.*, **30**, 3212–3222.
- Stammer, D., 1997: Global characteristics of ocean variability estimated from regional TOPEX/Poseidon altimeter measurements. *J. Phys. Oceanogr.*, **27**, 1743–1769.
- , 1998: On eddy characteristics, eddy transports, and mean flow properties. *J. Phys. Oceanogr.*, **28**, 727–739.
- Treguier, A. M., and B. L. Hua, 1988: Influence of bottom topography on stratified quasi-geostrophic turbulence in the ocean. *Geophys. Astrophys. Fluid Dyn.*, **43**, 265–305.
- Vallis, G. K., 1985: Remarks on the predictability properties of two- and three-dimensional flow. *Quart. J. Roy. Meteor. Soc.*, **111**, 1039–1047.
- , 1988: Numerical studies of eddy transport properties in eddy-resolving and parameterized models. *Quart. J. Roy. Meteor. Soc.*, **114**, 183–204.
- Visbeck, M., J. Marshall, T. Haine, and M. Spall, 1997: Specification of eddy transfer coefficients in coarse-resolution ocean circulation models. *J. Phys. Oceanogr.*, **27**, 381–402.
- Wardle, R., 2000: Representation of eddies in climate models by a potential vorticity flux. Ph.D. thesis, Massachusetts Institute of Technology–Woods Hole Oceanographic Institution Joint Program, 175 pp.